技術

網膜における内因性信号計測

角田和繁（つのだかずしげ）
東京医療センター感覚器センター視覚生理学研究室（〒152-8902 東京都目黒区東が丘2-5-1）
E-mail : tsunodakazushige@kankakuki.go.jp

実験のコツと注意点

網膜における内因性信号は大脳皮質における信号よりも一般に大きいが，測定にあたっては特に以下の点に注意する必要がある．

1. 眼球運動をはじめとする生体ノイズの抑制

麻酔下実験においても眼球の微小運動は大きなノイズ源となる．測定時には眼球運動を充分に制御するほか，点眼剤による散瞳，調節麻痺をしっかりと行う．血流の変化も測定に影響するため，心拍数・血圧などの条件を一定に保つように麻酔深度をコントロールする．

2. 可視観察光の影響の排除

視反応にともなう視物質の褪色変化により網膜の反射率は大きく上昇する．これは内因性信号とは逆の極性をもつ信号であるため，観察光としては赤外光を用い，褪色の影響を排除することが重要である．

背景

前号でも紹介された内因性信号による光学計測法は，神経活動にともなって神経組織の光反射率が変化する現象をとらえるもので，実験動物脳での機能的マッピングを行うのに非常に優れた方法である[1-4]．しかし，大脳皮質において光学計測法を行うためには脳表面を露出する必要があり，比較的大きな侵襲を伴うものである．したがってその臨床医学への応用は，てんかん患者に対する脳外科的手術時に行われる実験的なものに過ぎない[5]．一方，ヒトの網膜は内因性信号の計測に有利な特徴をいくつか備えている．まず，眼球の光学系（角膜，水晶体）を通して網膜を直接観察することができ，眼球自体が光学計測における理想的なチェンバーとして働くため，新たにチェンバーを作る手術的な侵襲がない．さらに，網膜外層では視細胞が密に一定方向に並んでいるため，光散乱変化による反射率変化をとらえやすい．

網膜，なかでもその中心に位置する黄斑部は，視力の維持に重要な部位であり，同時に臨床的に様々な疾患が起こりやすい部位でもある．内因性信号計測法が眼底での機能計測に応用できれば，網膜神経機能の客観的な評価法として網膜疾患の早期発見や早期治療につながることが期待される．

我々は内因性信号計測法の臨床応用を目指して，サル眼底における内因性信号計測を行っている（Functional Retinography : FRG）[6]．

脳における測定との相違

ヒトおよびサルの眼底は**図1a**に示すような特殊な解剖学的構造をしている．我々は測定を行う際に，眼底を中心窩網膜・周辺部網膜・視神経乳頭部の3部位に分類している．中心窩は錐体視細胞が密集している領域で毛細血管が存在しない（**図1b**）．周辺部網膜は典型的な10層構造をしており，杆体および錐体視細胞の他，双極細胞，神経節細胞，グリア細胞および網

1344-0128/06/¥100/頁/JCLS

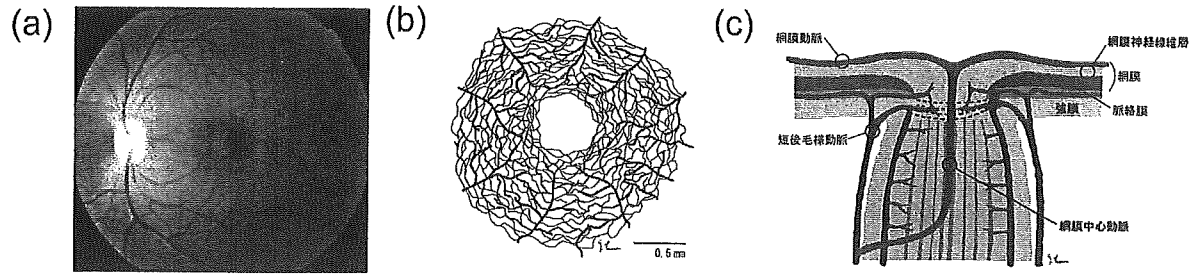

図1　眼底の構造

a：アカゲサルの眼底写真．b：中心窩毛細血管網の模式図．網膜中心部（300～500 μm）は無血管領域であり，錐体視細胞が密集している．c：視神経乳頭部の垂直断面模式図．ここには視細胞は存在せず，中心動静脈のほか毛細血管が豊富に存在する．(p.8，カラー図参照)

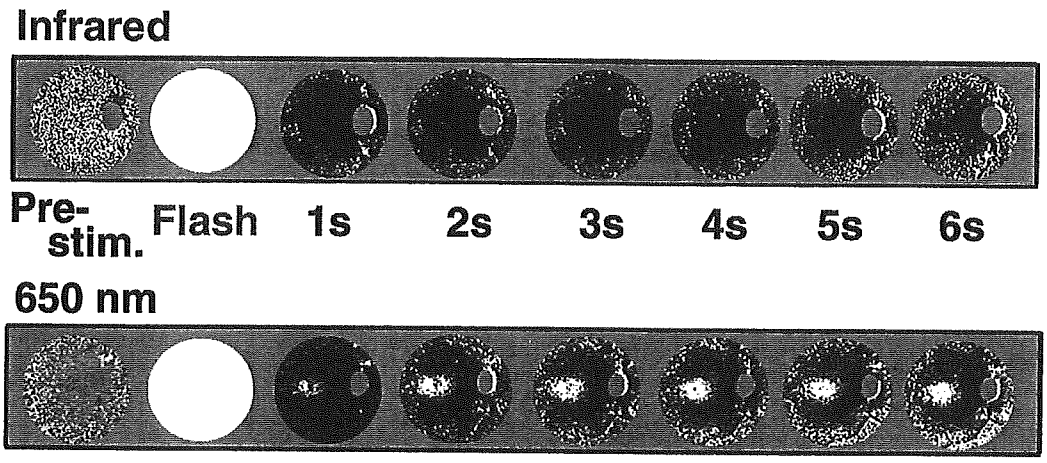

図2　赤外および可視観察光による内因性信号の違い

上段：赤外光観察下におけるフラッシュ刺激後の網膜反射率変化．網膜面全体の反射率低下（暗くなる変化）が見られる．下段：650 nmの観察光での網膜反射率変化．錐体視細胞の多い黄斑部付近では，視細胞の褪色変化により反射率が増加している（明るくなる変化）．

膜血管などが存在する．視神経乳頭部は神経節細胞の軸索の束であり，視細胞は存在しないが血管は豊富である（**図1c**）．これら3つの部位で記録される内因性信号は，それぞれ異なる信号起源を持っていると考えられる．

脳における内因性信号測定と最も異なる点は，受容体そのものが測定の対象である，ということである．すなわち刺激光のみならず観察光が内因性信号を惹起する可能性がある．また網膜固有の変化として，視細胞の褪色変化があげられる．褪色変化とは，光刺激によって視物質の異性化が起こるさい，視物質の光吸収特性が変化することである．吸収率のピークはより短波長側にシフトし，その結果光反射率の増加が観察される．これは内因性信号とは極性の異なる変化であり，観察光が可視光の場合は内因性信号と褪色変化という，2つの信号の和を計測していることになる（**図2**）[7,8]．このため神経活動のマッピングを行うさいには，観察光として近赤外光を用いる必要がある．

Ⅲ　実験方法

我々の施設で行っている標準的な実験方法について以下に述べる[6]．

1．実験動物

全身麻酔下のアカゲサルおよびニホンザルを用いて

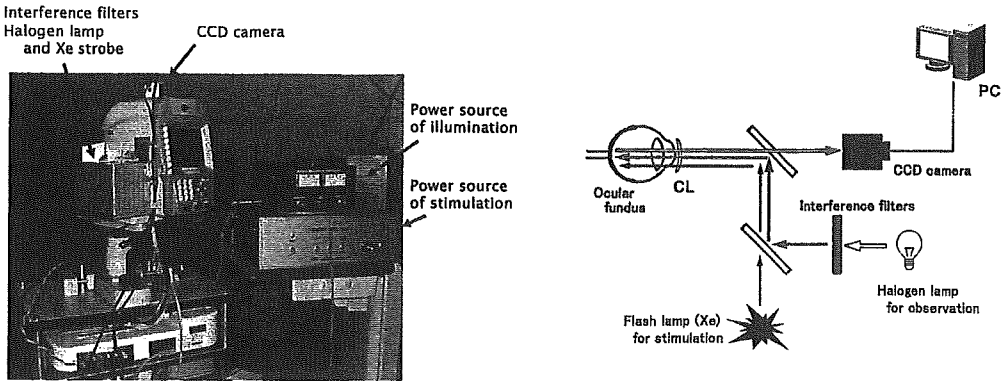

図3　網膜内因性信号計測システム（FRG）
左：計測装置の外観．右：実験セットアップの模式図．

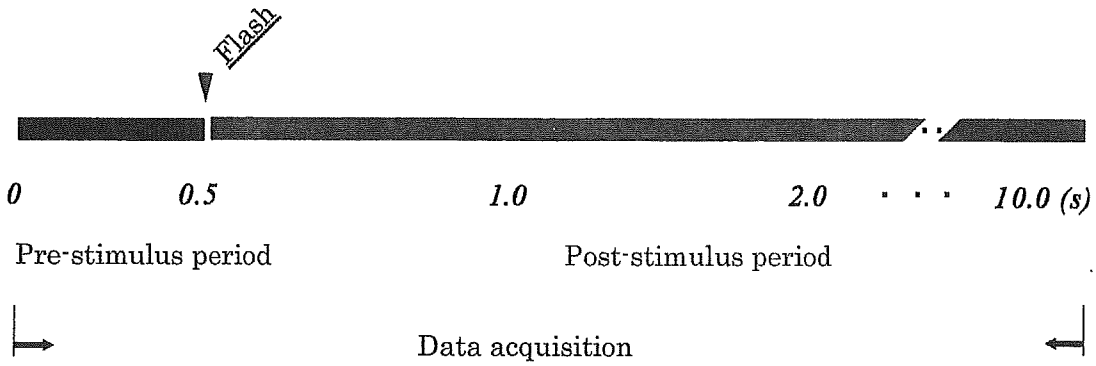

図4　測定開始からのタイムテーブル

いる．麻酔の導入には硫酸アトロピン（0.08 mg/kg），ドロペリドール（0.25 mg/kg）および塩酸ケタミン（5.0 mg/kg）の筋注を用いる．気管挿管後，筋弛緩剤として臭化ベクロニウムを持続静注（0.4～0.5 mg/kg/hr）し，笑気およびイソフルラン（1.0％）による吸入麻酔を行っている．散瞳，調節麻痺のため，トロピカミド・塩酸フェニレフリンの点眼を2時間おきに行う．

2. 測定システム

網膜反射率の計測には，市販されている眼底カメラの光学系，投光系を改良し，光刺激装置およびCCDカメラを付け加えたものを用いる（**図3**）．眼底観察用のハロゲン光は，干渉フィルター（800～900 nm）を透過して眼底後極部を照明する．解像度640×480，毎秒30フレームのCCDカメラによって眼底からの光反射率変化を持続的に記録する．測定開始から0.5秒後に眼底後極部全体を白色キセノンフラッシュ（1 ms）にて刺激する（**図4**）．一回の測定は通常5～10秒間行う．呼吸に伴う反射率変化の影響を減らすため，測定時には一時的に人工呼吸器を停止させている．

3. 内因性信号の計算方法

刺激前0.5秒間の平均画像の反射率と，刺激後の画像における反射率との比をピクセル毎に計算し，その比を256階調にスケーリングし画像化する．大脳皮質での測定では通常10～30回ほどの平均加算を要するが，網膜においては加算平均を行わないsingle trialでのマッピングが可能である．

Ⅲ　実際の測定結果

フラッシュによるびまん性刺激によって視細胞が活動すると，網膜全体の反射率が低下し画像上暗く描出される（**図5**）．この内因性信号は中心窩で最も強い．信号強度を疑似カラーで表示すると，明順応下では中

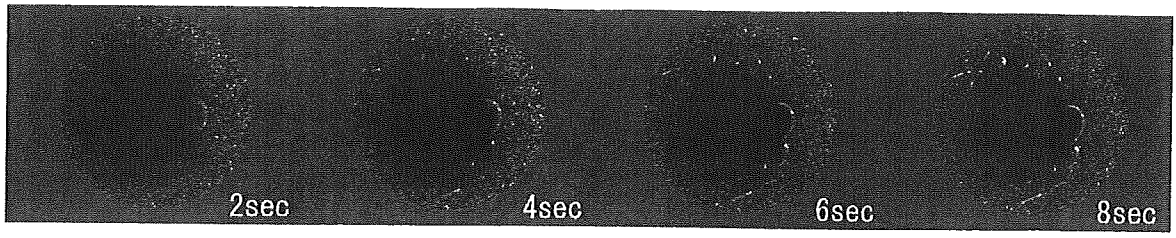

図5　赤外光観察下（800～900 nm）における網膜内因性信号

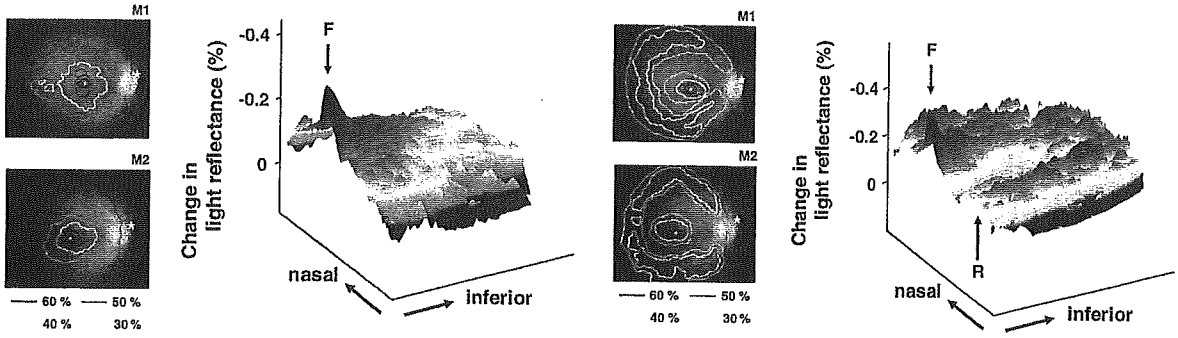

図6　網膜内因性信号のトポグラフィー

左図は明順応下，右図は暗順応下における記録．（白点は中心窩，＊印は視神経乳頭部を表す）

（p.8，カラー図参照）

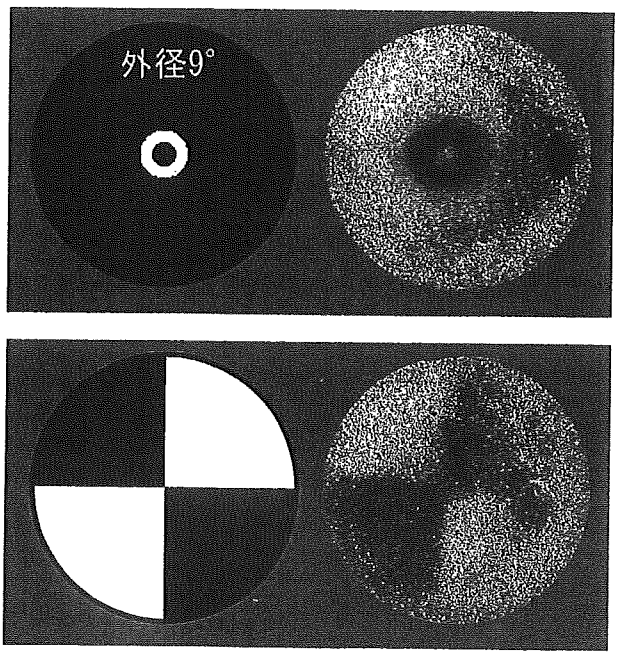

フラッシュ刺激の形状　　内因性信号

図7　刺激部位に対応した，網膜局所の内因性信号

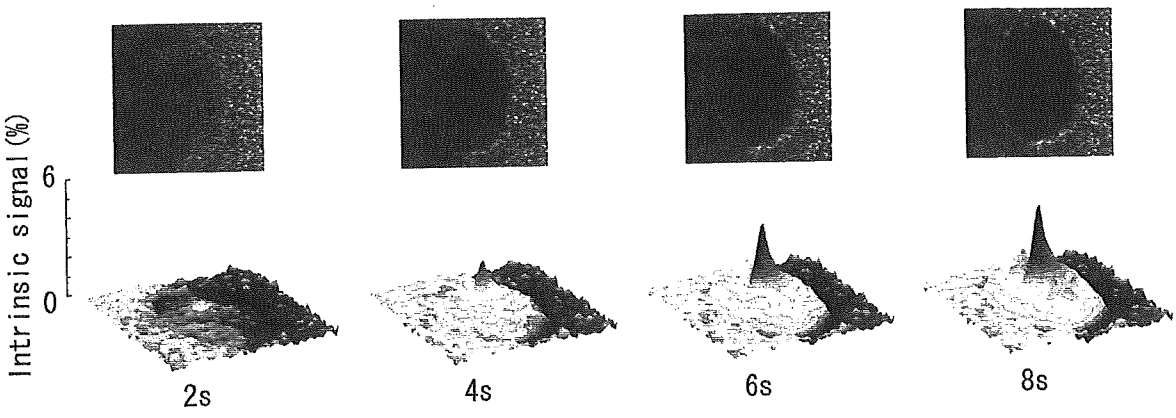

図8　視神経乳頭部におけるフラッシュ刺激後の内因性信号変化（上）および同部位のトポグラフィー（下）
（p.8，カラー図参照）

心窩に内因性信号の急峻なピークを認め，周辺部に向かって減少するが，暗順応下では中心窩に加えて周辺部にドーナツ状のピークを認める（**図6**）．内因性信号のピークは中心窩では錐体視細胞，周辺部では杆体視細胞の解剖学的な分布によく一致しており，網膜内因性信号の発生には視細胞が寄与していると思われる[9,10]．

また，網膜との共役面にフィルターを置いて局所フラッシュ刺激を行うと，刺激部位に相当する網膜のみから内因性信号を記録することができる（**図7**）．

一方，視神経乳頭部に注目すると，ここでは網膜面とは異なりフラッシュ刺激後にゆっくりと信号が強くなっていく（**図8**）．これは刺激後の血流増加を反映した光散乱強度変化と考えられ，中心動静脈に相当する視神経乳頭中央部に急峻なピークが見られる[11]．

まとめ

網膜における内因性信号の測定方法と実際の測定結果について簡単に説明した．測定にあたっては二つの画像の差を用いるため画像の偏位（眼球運動），光量の変化（瞳孔反応・光の入り具合）等様々な要因が障害となりうる．現在のところ，ヒト網膜において詳細なマッピングを行うまでには至っていない．今後，測定技術および解析方法等の改良により客観的網膜機能イメージング法としての臨床応用が可能となれば，さまざまな網膜疾患の早期発見・早期治療に役立つものと確信している．

参考文献

1) Grinvald A, et al : Functional architecture of cortex revealed by optical imaging of intrinsic signals. Nature **324** : 361-364, 1986.
2) Bonhoeffer T, Grinvald A : Optical Imaging Based on Intrinsic Singals: The Methodology. In: Toga AW, Mazziotta JC, eds. Brain Mapping. San Diego: Academin Press; 55-97, 1996.
3) Tsunoda K, et al : Complex objects are represented in macaque inferotemporal cortex by the combination of feature columns. Nat Neurosci **4** : 832-838, 2001.
4) Fukuda M, et al : Localization of activity-dependent changes in blood volume to submillimeter-scale functional domains in cat visual cortex. Cereb Cortex **15** : 823-833, 2005.
5) Haglund MM, et al : Optical imaging of epileptiform and functional activity in human cerebral cortex. Nature **358** : 668-671, 1992.
6) Tsunoda K, et al : Mapping Cone- and Rod-Induced Retinal Responsiveness in Macaque Retina by Optical Imaging. Invest. Ophthalmol **45** : 3820-3826, 2004.
7) Kilbride PE, et al : Determination of human cone pigment density difference spectra in spatially resolved regions of the fovea. Vision Res **23** : 1341-1350, 1983.
8) Elsner AE, et al : Mapping cone photopigment optical density. J Opt Soc Am A **10** : 52-58, 1993.
9) Osterberg G : Topography of the layer of rods and cones in the human retina. Acta ophthalmol **13** : 6-9, 1935.
10) Curcio CA, et al : Distribution of cones in human and monkey retina: individual variability and radial asymmetry. Science. **236** : 579-582, 1987.
11) Riva CE, et al : Flicker-evoked responses of human optic nerve head blood flow: luminance versus chromatic modulation. Invest Ophthalmol **42** : 756-762, 2001.

日本視能訓練士協会誌　第３５巻

網膜神経活動のイメージング

― 網膜内因性信号計測法 ―

A novel imaging technique of neural function in retina
-Intrinsic signal imaging of retina-

角田和繁（つのだかずしげ）
東京医療センター臨床研究センター視覚生理学研究室
〒152-8902　東京都目黒区東が丘 2-5-1
tsunodakazushige@kankakuki.go.jp

（キーワード）　網膜内因性信号計測法、イメージング、網膜機能評価

視覚的機能を他覚的に評価することは、眼疾患の早期発見および治療効果の判定のために基本的かつ重要な課題である。そのために眼科における画像診断技術（イメージング）は近年めざましい進歩をとげてきたが、それらは主に解剖学的構造の把握を目的としており、視細胞をはじめとする網膜の神経活動を捉えることはできない。我々が開発した網膜内因性信号計測法は、非侵襲的な網膜神経機能のイメージング法であり、神経活動にともなって神経組織の微細構造や光反射率が変化する現象を利用したものである。この技術により、従来は不可能であった錐体視細胞、杆体視細胞の機能的マッピングを、高い解像度で行うことができるようになった。動物実験における信号の閾値は網膜電図（ＥＲＧ）のｂ波とほぼ同等であることが示されており、現在ヒトでの計測が可能なように開発を行っている。このイメージング法が実現すれば、様々な網膜疾患において精度の高い他覚的機能評価が可能になると期待されている。

＜はじめに＞

眼科における画像診断技術は近年めざましい進歩をとげてきた。たとえば光干渉断層計（OCT）は、検眼鏡によって捉えることのできない網膜微細構造の観察を可能にするものであり、網膜疾患の診断、治療に関する従来の常識を一変させるほど臨床応用価値の高いものである。しかし OCT や、走査型レーザー検眼鏡（SLO）などの画像診断法は、解剖学的構造の把握を目的としており、これによって視細胞をはじめとする網膜の神経活動を捉えることはできない。したがって、網膜機能（神経活動）の他覚的評価のためには、電気生理学的検査である網膜電図（ERG）が今でも主要な役割を果たしている。

網膜、なかでもその中心に位置する黄斑部は、視力の維持のために重要な部位であり、同時に臨床的に様々な疾患が起こりやすい部位でもある。我々のグループでは、ERG とはまったく異なるしくみで網膜の神経活動を非侵襲的にイメージングする方法を開発し、新たな眼科検査法としての実用化に向けた研究を行っている（網膜内因性信号計測法、Functional Retinography）。内因性信号計測法が眼底における機能計測に応用できれば、網膜神経機能の客観的な評価法として疾患の早期発見や早期治療につながることが期待される。本項では網膜内因性信号計測法がいかなる検査法であるか、またこの検査法の展望について紹介したい。

＜網膜内因性信号計測法とは＞

神経活動にともなって神経組織の微細構造や光反射率が変化する現象は古くから知られている[1)]。特に、神経活動にともなう代謝変化を光の反射率変化として捉える計測法は内因性信号計測法（Intrinsic Signal Imaging）と呼ばれ、最近の脳科学の進歩に大きく貢献してきた[2-5)]。実際の計測法は、神経組織を CCD カメラでイメージングし、刺激前と刺激後の画像を重ね合わせて比較するという非常に単純なものである。刺激後に画像の明るさが変化している部分が神経活動の起きた領域に相当し、通常は神経活動の高い領域がより暗く見える。信号の起源として、神経活動にともなう光散乱変化や血中ヘモグロビン飽和度の変化などが考えられている（図１）。

しかし、大脳皮質において光学計測法を行うためには脳表面を露出する必要があり、比較的大きな侵襲を伴うものである。したがってその臨床医学への応用は、てんかん患者に対する脳外科的手術時に行われる実験的なものに過ぎない[6)]。一方、ヒトの網膜は内因性信号の計測に有利な特徴をいくつか備えている。まず、眼球の光学系（角膜、水晶体）を通して網膜を直接観察することができ、眼球自体が光学計測における理想的な観察用チェンバーとして働くため、手術的な侵襲が必要ない。さらに、網膜外層では視細胞が密に一定方向に並んでいるため、光散乱変化による反射率変化をとらえやすい。筆者はこの技術の眼科分野への応用に着目し、早くから網膜における実験を行ってきた[7)]。

＜測定方法＞

開発のための動物実験では、ヒトとほぼ同じ解剖学的構造を持つニホンザル、アカゲザルの眼底を用いている。

全身麻酔下において非動化した眼底を、眼底カメラを改良した観察系を用いて CCD カメラでモニターする（図 2）。眼底観察用のハロゲン光は、干渉フィルター（800−900nm）を透過して眼底後極部を照明する。解像度 640×480、毎秒 30 フレームの CCD カメラによって眼底からの光反射率変化を持続的に記録する。測定開始から 0.5 秒後に眼底後極部全体を白色キセノンフラッシュ（1ms）にて刺激する。一回の測定は通常５－１０秒間行う。

刺激前 0.5 秒間の平均画像の反射率と、刺激後の画像における反射率との比をピクセル毎に計算し、その比を 256 階調にスケーリングし画像化する。大脳皮質での測定では通常１０－３０回ほどの平均加算を要するが、網膜においては加算平均を行わない、single trial でのマッピングが可能である。

＜結果＞

フラッシュによるびまん性刺激によって視細胞が活動すると、網膜全体の反射率が低下し画像では暗く描出される（図３）。この内因性信号は刺激後 150m s にピークを持つ早い反応で、中心窩で最も強い。信号強度を疑似カラーで表示すると、明順応下では中心窩に内因性信号の急峻なピークを認め、周辺部に向かって減少するが、暗順応下では中心窩に加えて周辺部にドーナツ状のピークを認める（図４）。内因性信号のピークは中心窩では錐体視細胞に、周辺部では杆体視細胞の解剖学的な分布（rod ring）によく一致しており、網膜内因性信号の発生には視細胞が大きく寄与していると思われる[8-9]。

さらに、視神経乳頭部に注目すると、ここでは網膜面とは異なりフラッシュ刺激後にゆっくりと信号が強くなっていく。これは刺激後の血流増加を反映した光散乱強度変化と考えられ[10]、中心動静脈に相当する視神経乳頭中央部に急峻なピークが見られる（図５）。

なお、同一の刺激系を用いて角膜電極より暗順応ＥＲＧを記録し、内因性信号と比較すると、黄斑部を除く網膜面および視神経乳頭における内因性信号の閾値は、ＥＲＧの b 波とほぼ同一であることが分かった。これは、網膜内因性信号計測法が非常に感度の高い神経機能計測法であることを示している。

＜まとめ＞

内因性信号計測法の利点は、赤外光の反射率変化を計測するために非侵襲的であること、空間分解能が高いこと（理論上は眼底写真に相当）、測定時間が短いことなどである。問題点としては、ヒトの測定時に生じる固視微動等により、画質が著しく低下することであり、現在それを克服すべく研究を行っている。将来臨床応用が可能になれば黄斑変性症や網膜色素変性症など様々な網膜疾患において精度の高い他覚的機能評価が可能になると期待されている。

さらに網膜内因性信号計測法以外にも、近年は OCT を利用して神経機能評価を行おうという研究も行われている。これは 2002 年に理化学研究所の Maheswari らによって初めて提唱された Functional OCT[11] という概念であり、網膜における応用に向けた研究がすでにいくつかの国の研究機関で行われている。網膜の神経機能をイメージングするという研究は新しい診断法として高く注目されており、将来はＥＲＧと並ぶ新たな客観的機能評価法が確立される日が来るに違いない。

<参考文献>

1) Cohen L. Changes in neuron structure during action potential propagation and synaptic transmission. Physiol Rev. 53: 373-418, 1973

2) Grinvald A, Lieke E, Frostig RD, Gilbert CD, Wiesel TN. Functional architecture of cortex revealed by optical imaging of intrinsic signals. Nature, 1986;324:361-364.

3) Bonhoeffer T, Grinvald A. Optical Imaging Based on Intrinsic Singals: The Methodology. In: Toga AW, Mazziotta JC, eds. Brain Mapping. San Diego: Academin Press; 1996:55-97.

4) Tsunoda K, Yamane Y, Nishizaki M, Tanifuji M. Complex objects are represented in macaque inferotemporal cortex by the combination of feature columns. Nat Neurosci. 2001;4:832-8.

5) Fukuda M, Maheswari RU, Homma R, Matsumoto M, Nishizaki M, Tanifuji M. Localization of activity-dependent changes in blood volume to submillimeter-scale functional domains in cat visual cortex. Cereb Cortex. 2005 Jun;15(6):823-33.

6) Haglund MM, Ojemann GA, Hochman DW. Optical imaging of epileptiform and functional activity in human cerebral cortex. Nature 1992 358: 668-671.

7) Tsunoda K, Oguchi Y, Hanazono G, and Tanifuji M. Mapping Cone- and Rod-Induced Retinal Responsiveness in Macaque Retina by Optical Imaging. Invest. Ophthalmol. Vis. Sci. 2004 45: 3820-3826.

8) Osterberg G. Topography of the layer of rods and cones in the human retina. Acta ophthalmol. 1935;13:6-97.

9) Curcio CA, Sloan KR, Jr., Packer O, Hendrickson AE, Kalina RE. Distribution of cones in human and monkey retina: individual variability and radial asymmetry. Science. 1987;236:579-82.

10) Riva CE, Falsini B, Logean E. Flicker-evoked responses of human optic nerve head blood flow: luminance versus chromatic modulation. Invest Ophthalmol Vis Sci. 2001;42:756-62.

11) Maheswari RU et al. Implementation of optical coherence tomography (OCT) in visualization of functional structures of cat visual cortex. Opt. Comm. 202: 47-54, 2002

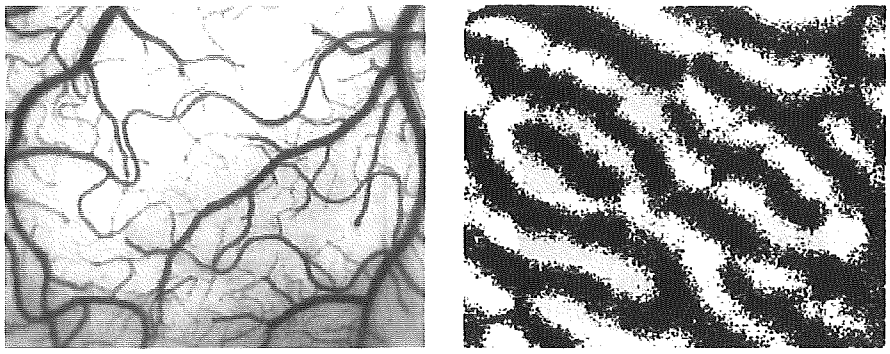

図１．（左）アカゲサル第一次視覚野の皮質表面。（右）内因性信号計測によって描出された同部位の眼優位性コラム。黒い帯が右眼の入力を受けて神経活動が高まっている領域。

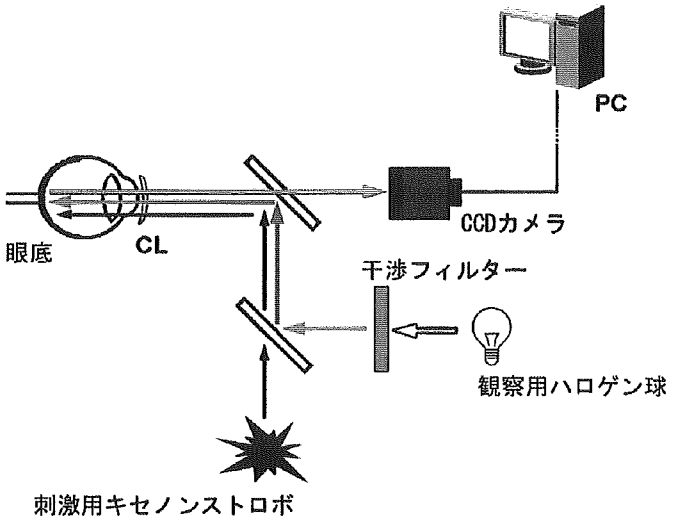

図２．実験セットアップの模式図。

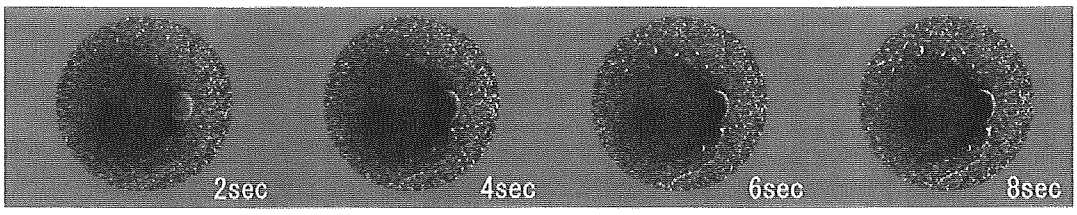

図３．赤外光観察下（800－900nm）における網膜内因性信号。後極部が暗く変化しているのが分かる。

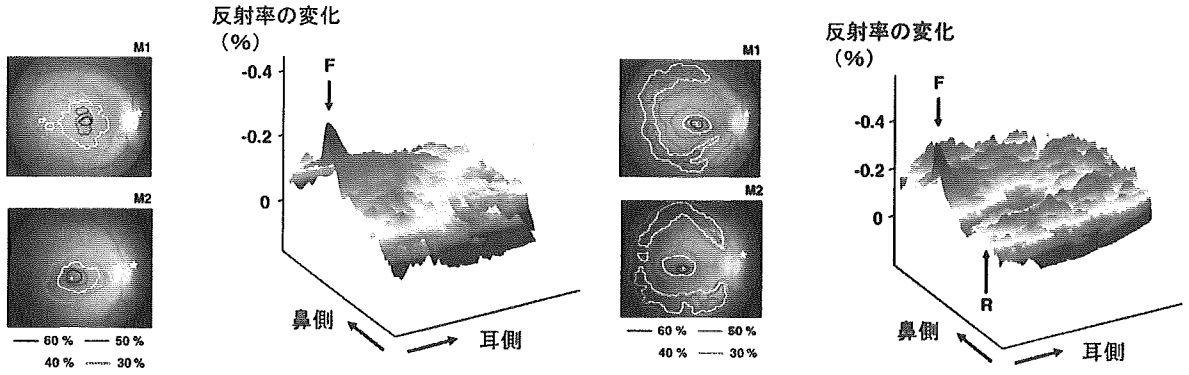

図４．網膜内因性信号のトポグラフィー。左図は明順応下、右図は暗順応下における記録。等高線は反応のピークに対する相対値を示す。(白点：中心窩、　＊印：視神経乳頭部、　F：Fovea、　R：Rod ring　)

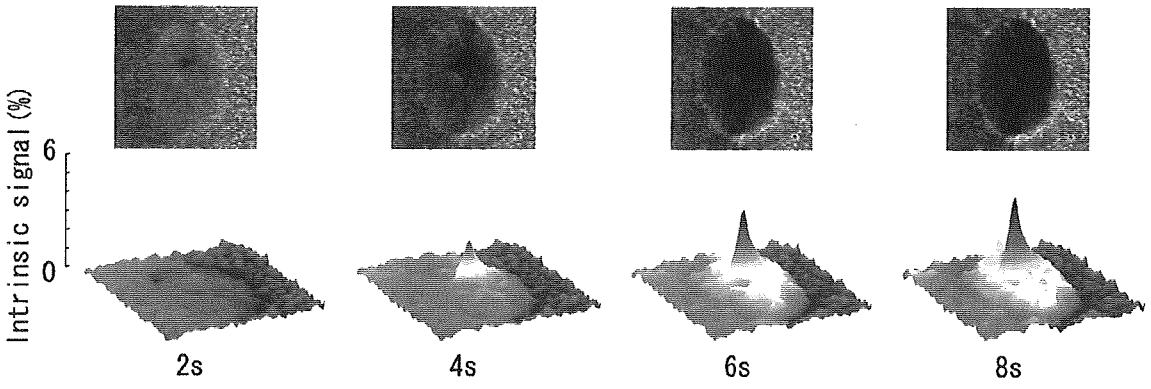

図５．視神経乳頭部におけるフラッシュ刺激後の内因性信号変化(上)および同部位のトポグラフィー(下)。

tion：preliminary report. J Cataract Refract Surg **25**：1394-1399, 1999
15) Inan UU, Ozturk F, Kaynak S et al：Prevention of posterior capsule opacification by intraoperative single-dose pharmacologic agents. J Cataract Refract Surg **27**：1079-1087, 2001
16) Kim JT, Lee do H, Chung KH et al：Inhibitory effects of salmosin, a disintegrin, on posterior capsular opacification in vitro and in vivo. Exp Eye Res **74**：585-594, 2002

Column

新たな網膜機能の画像化

すでに本書の各項で取り上げられてきたように，近年の眼科画像診断技術にはめざましい進歩があった。特に光干渉断層計（OCT）は，検眼鏡によって捉えることのできない網膜微細構造の観察を可能にするものであり，網膜疾患の診断，治療に関する従来の常識を一変させるほど臨床応用価値の高いものであった。しかしOCT，走査型レーザー検眼鏡（SLO）などの画像診断法は，いうまでもなく解剖学的構造の把握を目的としており，これによって視細胞をはじめとする網膜の神経活動を捉えることはできない。したがって，網膜の機能（神経活動）の他覚的評価のためには，電気生理学的検査である網膜電図（ERG）が主要な役割を果たしている。

一方，神経活動に伴って神経組織の微細構造や光反射率が変化する現象は古くから知られており[1]，光を使って生体脳の神経活動を測定する光学計測法（optical imaging）が1990年頃よりさかんに行われてきた[2,3]。これは，特に内因性信号計測法（intrinsic signal imaging）とも呼ばれ，電位感受性色素などのケミカルプローブを使わない神経活動のイメージング法である。実際の計測法は，神経組織をCCDカメラでイメージングし，刺激前と刺激後の画像を重ね合わせて比較するという非常に単純なものである（差分画像の作成）。刺激後に画像の明るさが変化している部分が神経活動の起きた領域に相当し，通常は神経活動の高い領域がより暗くみえる。信号の起源として，神経活動に

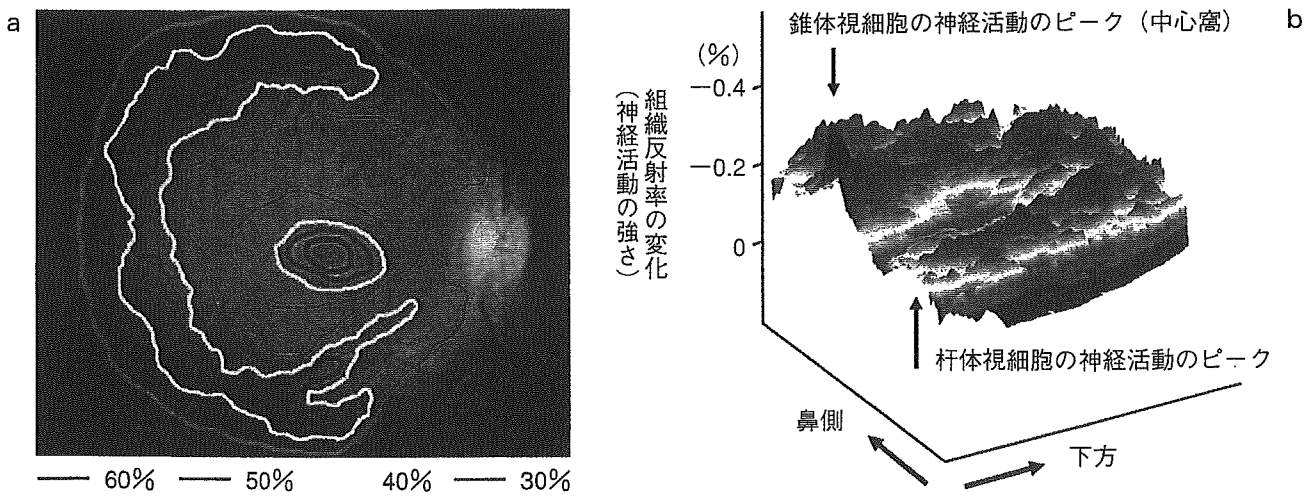

図1 Functional retinographyによる網膜神経活動のトポグラフィ（サル，暗順応下）
a：中心窩（黒点）に対する相対的信号強度，b：下方網膜の断面図。

17) Hepsen IF, Bayramlar H, Gultek A et al：Caffeic acid phenethyl ester to inhibit posterior capsule opacification in rabbits. J Cataract Refract Surg **23**：1572-1576, 1997
18) Tarsio JF, Kelleher PJ, Tarsio M et al：Inhibition of cell proliferation on lens capsules by 4197X-ricin A immunoconjugate. J Cataract Refract Surg **23**：260-266, 1997
19) 松島博之：Drug Delivery IOL. あたらしい眼科 **21**：607-613, 2004

伴う光散乱変化や血中ヘモグロビン飽和度の変化などが考えられている。

筆者はこの技術の網膜への応用に着目し，大脳皮質での計測の経験を活かして早くから実験を行ってきた(網膜内因性信号計測法 functional retinography：FRG[4])。FRG の利点は，赤外光の反射率変化を計測するために非侵襲的であること，空間分解能が高いこと(理論上は眼底写真に相当)，測定時間が短いことなどである。図 1 は，暗順応後のアカゲザル眼底を 810 nm の近赤外光で観察し，白色フラッシュ刺激後の反射率変化を空間的に表したものである。図 1b の 3D マップで高くなっている部分が神経活動の強く起きた領域で，解剖学的には錐体視細胞の密集部（中心窩）および杆体視細胞の密集部 (rod ring) に相当している。記録しているのはフラッシュ刺激に対する網膜の反応であるが，ERG とは異なり主な信号源が網膜外層であることが特徴である。このように FRG は，網膜の神経機能を高解像度，短時間でイメージングする方法であり，網膜の新しい機能評価法として今後の臨床応用に強く期待がもたれている。

さらに，OCT を利用して神経機能評価を行おうという研究も始められている。OCT で神経活動を捉えるという概念は 2002 年に理化学研究所の Maheswari ら[5]によって初めて提唱された (functional OCT)。すなわち刺激によって神経組織に微細構造変化が生じ，それに伴う光散乱変化によって OCT 信号が局所的に変化するというものである。オーストリアの Drexler らのグループは，ウサギの網膜標本にフラッシュ刺激を与えることにより，網膜各層の OCT 信号強度が経時的に変化していることを示している。将来的には，網膜層状構造のどの部位で機能的異常が生じたかを検出できる可能性がある。

以上，新たな網膜機能の画像化への試みとして，FRG と functional OCT を取り上げてみた。いずれもこれまで不可能であった神経活動の画像化を目ざす新しい技術であり，将来は網膜の解剖学的評価ばかりでなく，精度の高い他覚的機能評価が可能になると期待されている。

文　献

1) Cohen L：Changes in neuron structure during action potential propagation and synaptic transmission. Physiol Rev **53**：373-418, 1973
2) Grinvald A, Lieke E, Frostig RD et al：Functional architecture of cortex revealed by optical imaging of intrinsic signals. Nature **324**：361-364, 1986
3) Tsunoda K, Yamane Y, Nishizaki M et al：Complex objects are represented in macaque inferotemporal cortex by the combination of feature columns. Nat Neurosci **4**：832-838, 2001
4) Tsunoda K, Oguchi Y, Hanazono G et al：Mapping cone-and rod-induced retinal responsiveness in Macaque retina by optical imaging. Invest Ophthalmol Vis Sci **45**：3820-3826, 2004
5) Maheswari RU, Takaoka H, Homma R et al：Implementation of optical coherence tomography (OCT) in visualization of functional structures of cat visual cortex. Opt Comm **202**：47-54, 2002

角田和繁（東京医療センター感覚器センター）

Cerebral Cortex June 2005;15:823-833
doi:10.1093/cercor/bhh183
Advance Access publication September 30, 2004

Localization of Activity-dependent Changes in Blood Volume to Submillimeter-scale Functional Domains in Cat Visual Cortex

Mitsuhiro Fukuda[1,2], Uma Maheswari Rajagopalan[1], Ryota Homma[1], Madoka Matsumoto[1,3], Makoto Nishizaki[1,4] and Manabu Tanifuji[1]

[1]Laboratory for Integrative Neural Systems, RIKEN Brain Science Institute, 2-1 Hirosawa, Wako-shi, Saitama, 351-0198, Japan
[2]Present address: Department of Neurobiology, Brain Imaging Research Center, University of Pittsburgh, 3025 East Carson Street, PA 15203, USA
[3]Present address: Laboratory for Cognitive Brain Mapping, RIKEN Brain Science Institute, 2-1 Hirosawa, Wako-shi, Saitama, 351-0198, Japan
[4]Present address: Advanced Technology Research Laboratories, Matsushita Electric Industrial Co., Ltd., 3-10-1 Higashimita, Tama-ku, Kawasaki-shi, 214-8501, Japan

We have examined whether blood volume changes induced by neural activation are controlled precisely enough for us to visualize the submillimeter-scale functional structure in anesthetized and awake cat visual cortex. To activate the submillimeter-scale functional structures such as iso-orientation domains in the cortex, visual stimuli (gratings) were presented to the cats. Two methods were used to examine the spatial precision of blood volume changes including changes in total hemoglobin content and changes in plasma volume: (i) intrinsic signal imaging at the wavelength of hemoglobin's isosbestic point (569 nm) and (ii) imaging of absorption changes of an intravenously injected dye. Both measurements showed that the visual stimuli elicited stimulus-nonspecific and stimulus-specific blood volume changes in the cortex. The former was not spatially localized, while the latter was confined to iso-orientation domains. From the measurement of spatial separation of the iso-orientation domains, we estimated the spatial resolution of stimulus-specific blood volume changes to be as high as 0.6 mm. The changes in stimulus-nonspecific and -specific blood volume were not linearly correlated. These results suggest the existence of fine blood volume control mechanisms in the capillary bed in addition to global control mechanisms in arteries.

Keywords: cerebral blood flow, functional MRI, hemodynamic response, intrinsic signal imaging, orientation column, spectroscopic analysis

Introduction

The activation of cortical neurons elicits changes in light reflection from an exposed cortical surface. The measurement of these light reflection changes (intrinsic signals) enables cortical functional structures to be visualized at submillimeter-scale spatial resolution and provides profound insights into cortical functions in visual areas (Grinvald *et al.*, 1986; Ts'o *et al.*, 1990; Bonhoeffer and Grinvald, 1991, 1993; Malonek *et al.*, 1994; Roe and Ts'o, 1995; Wang *et al.*, 1996, 1998; Ghose and Ts'o, 1997; Tsunoda *et al.*, 2001).

Circumstantial evidence suggests that hemodynamic responses, such as changes in deoxyhemoglobin (Hbr) concentration and blood volume changes, are the major sources of intrinsic signals at visible wavelengths (Frostig *et al.*, 1990; Bonhoeffer and Grinvald, 1996; Malonek and Grinvald 1996). Decreases in light reflection (i.e. increases in light absorption) at 600–630 nm, where the absorption coefficient of Hbr is 5–10 times higher than that of oxyhemoglobin (HbO_2) (Fig. 1 inset), suggest that increases in Hbr concentration are accompanied by the oxygen consumption of activated neurons (Silver, 1978; Sibson *et al.*, 1998; Thompson *et al.*, 2003). The decrease in light reflection at the wavelength where the absorption coefficient of HbO_2 equals that of Hbr (i.e. hemoglobin's isosbestic point) suggests that an increase in total hemoglobin (Hbt) concentration (blood volume change) is another component of the signal. In addition to these hemodynamic components, activity-dependent light scattering (Ls) changes (MacVicar and Hochman, 1991; Holthoff and Witte, 1996) may also be involved in intrinsic signals at wavelengths >700 nm, at which the absorption coefficients of both HbO_2 and Hbr are relatively small (Maheswari *et al.*, 2003).

Since hemodynamic responses are the basis of modern functional brain imaging techniques such as positron emission tomography (PET) and functional magnetic resonance imaging (fMRI), it is very important to characterize their spatial and temporal properties. Analyses of intrinsic signals at visible wavelengths provide clues that can lead to an understanding of these properties. Malonek and Grinvald (1996) applied spectroscopy to the analysis of intrinsic signals in the cat visual cortex, and found that increases in Hbr concentration were confined to iso-orientation domains, but increases in HbO_2 concentrations were less localized. These results suggest that blood inflow to an activated area is not strongly confined to submillimeter-scale functional domains. However, Duong *et al.* (2001) have recently demonstrated using cerebral-blood-flow (CBF)-based fMRI that blood flow changes are strongly localized to iso-orientation domains in the cat visual cortex. Similarly, an earlier work suggested that blood volume changes associated with changes in blood inflow are localized in active domains (Frostig *et al.* 1990). Thus, the spatial specificities of blood flow changes and associated blood volume changes are still unresolved. In particular, because of the lack of detailed examinations, the specificity of blood volume changes remains unconfirmed. Here, we characterized spatial and temporal patterns of blood volume changes in the cat visual cortex using two methods: (i) intrinsic signal imaging at the wavelength of hemoglobin's isosbestic point, and (ii) imaging of absorption changes of an intravenously injected absorption dye.

Materials and Methods

Eighteen cats (2–6 months of age, 1.0–3.3 kg) were used under anesthesia; five of the animals were also used in the awake state. All procedures were conducted following the 'Guiding Principles for the Care and Use of Animals in the Field of Physiological Sciences' (The

Cerebral Cortex V 15 N 6 © Oxford University Press 2004; all rights reserved

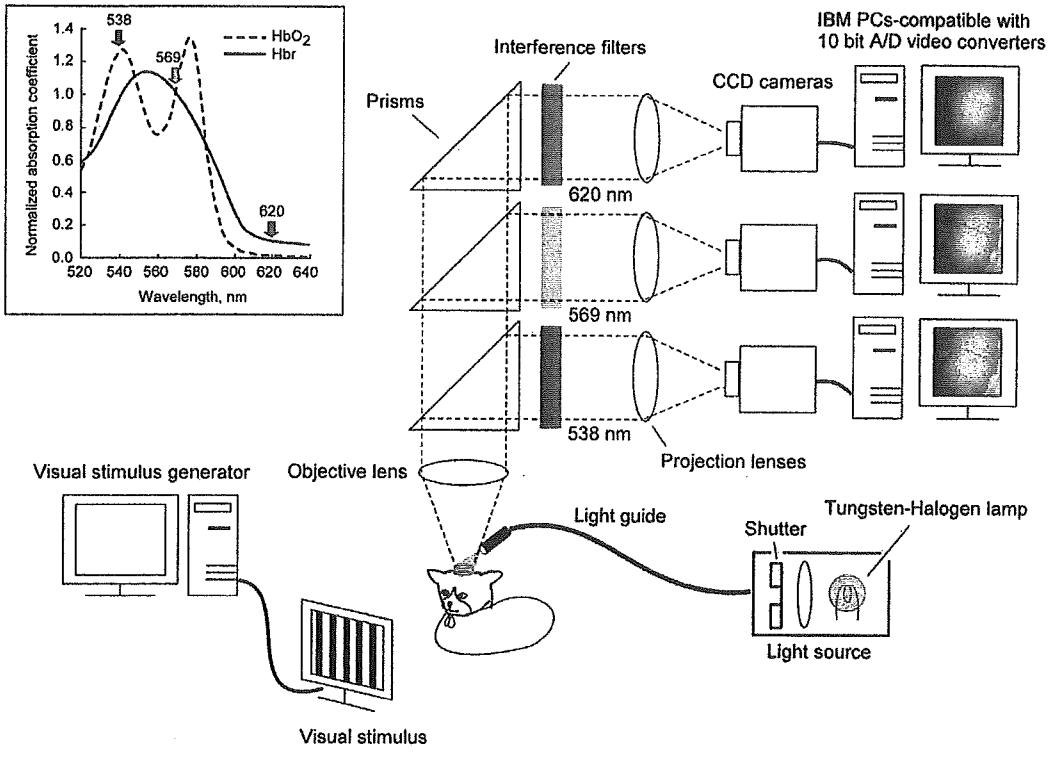

Figure 1. Scheme of the multiple wavelength imaging system. The cortical surface is illuminated with white light. Reflected light is collected by an objective lens and divided into three light paths by prisms. Each beam passes through an interference filter and is focused onto the target plane of the video cameras by projection lenses. The inset on the upper left corner shows absorption spectra of HbO_2 and Hbr. The arrows indicate central wavelengths of the three filters we used (538, 569 and 620 nm). The absorption coefficients of HbO_2 and Hbr at different wavelengths were obtained from *in vitro* experiments and normalized to the absorption coefficient at 569 nm. The normalized coefficients of HbO_2 and Hbr at 538 nm were 1.23 and 0.91 respectively. Similarly, at 620 nm the normalized coefficients of HbO_2 and Hbr were 0.01 and 0.11 respectively.

Physiological Society of Japan), and with the approval of the RIKEN Committee on Animal Research.

Animal Preparations

Cats were initially anesthetized with an inhalation of isoflurane (2-2.5%) in a mixture of 50% N_2O and 50% O_2. After tracheal cannulation, anesthesia was maintained with a mixture of 70% N_2O and 30% O_2 supplemented with 1-2% isoflurane. The cephalic vein was catheterized and neuromuscular blockade was carried out by continuous infusion of pancuronium bromide (0.2 mg/kg/h) mixed with dexamethazone (0.05 mg/kg/h) and 7.5% glucose in lactose-containing Ringer's solution. The cats were then artificially ventilated. To prevent the cornea from drying, contact lenses were fitted to the eyes. We continuously monitored rectal temperature, electroencephalogram (EEG), electrocardiogram (ECG), and expired CO_2 to assess the depth of anesthesia. Rectal temperature was maintained at 37.5-38.5 °C with a feedback-regulated heating pad system. The expired CO_2 was maintained between 3.0 and 4.0%.

On the first day of recording, a cat was placed in a stereotaxic apparatus (SN-3N, Narishige). Under aseptic surgery, we first attached with dental acrylic cement a metal post to fix its head and a stainless steel chamber (18 mm inner diameter, Nakazawa-Seisaku, Japan) for optical imaging to the skull. The metal post was placed approximately above the bregma: The chamber was placed such that it included area 17 or the border between areas 17 and 18 (in Horsley-Clarke coordinates, approximately A5-P10 for area 17 and A10-P5 for the border between areas 17 and 18). We then performed craniotomy inside the chamber, and resected the dura mater. The inside of the chamber was then filled with 1.5-2.0% agarose (Agarose-HGS, gel strength 1.5%; Nacalai Tesque, Japan) containing dexamethazone (0.1 mg) and an antibiotic (gentamicin, 0.25 mg). Finally, the chamber was covered with a round glass coverslip and sealed with a screw-top lid including a silicone gasket. We could observe the cortical surface clearly through the glass coverslip and could visualize the same functional structures repeatedly for 2-3 weeks without cleaning the inside of the chamber. After the surgery and the recordings, an appropriate antibiotic (cefodizime sodium, 60 mg/kg i.m.) was administered to the cat before returning the animal to its home cage.

During recordings on the first and subsequent days, the cat's head was immobilized with a head post instead of ear bars. Pupils were dilated by applying 0.5% tropicamide and 0.5% phenylephrine hydrochloride. The isoflurane concentration was maintained at 0.5-1.0% during the recordings. The other conditions were the same as those in the initial surgery described above.

Visual Stimuli

Square wave gratings (white: 8 cd/m^2; black: 0 cd/m^2) were generated with a VSG2/3 graphics video board (Cambridge Research Systems, Rochester, UK), controlled by homemade software, and were presented on a monitor screen (640 × 480 pixels and 100 Hz refresh rate, GDM-20SE3T, Sony). The spatial frequency and the drifting velocity of the gratings were 0.5 cycles/deg and 4 deg/s for area 17, and 0.15 cycles/deg and 15 deg/s for area 18 (Bonhoeffer *et al.*, 1995). The drifting direction was reversed every 0.5 s during a 2 s stimulus presentation. Two or four stimuli [orientations, 0° (horizontal), 45°, 90° and 135°] together with a blank screen (homogenous gray, 4 cd/m^2) as a control were presented in a pseudorandom order. In the experiment using awake cats, we used stationary grating patterns flickering at 5 Hz (8 Hz in one cat) to minimize the effect of eye movements following the grating motion. The same flickering gratings were also used in the examination of the same cats under anesthesia for comparison.

The center of a cat's visual field was estimated by projecting images of optic disks and patterns of surrounding vessels onto the monitor screen in front of the cat. The screen was placed at a distance ranging from 20 to 40 cm, where the best focus of the optic disks and the patterns of surrounding vessels were obtained for each cat. At these distances the size of the screen corresponded to 43°-86° (width) × 36°-71° (height)

of the cat's visual field. In the experiment with awake cats, the screen was placed 20 cm in front of the animals.

Optical Imaging of Intrinsic Signals

We developed a multiple wavelength imaging system equipped with three identical cameras (Sanso-Seisaku, Japan) that enabled us to simultaneously record intrinsic signals at three different wavelengths (Fig. 1). We used two sets with the same configuration: one was equipped with CID-2221D video cameras (CIDTEC, Liverpool, NY), and the other was equipped with CS8310 video cameras (Tokyo Electric Industry, Japan). The exposed cortical surface was illuminated with white light using eight fiber optic bundles placed around the chamber, which were connected to two tungsten-halogen bulbs (82 V, 300 W; Philips) driven by stabilized DC power supplies (PD110-5D; Kenwood, Japan). The duration of exposure of the cortical surface to the light was restricted to 10 s using a mechanical shutter, which opened 2 s before starting image acquisition. Reflected light from the cortical surface was collected by an objective lens, and divided into three separate paths by prisms. Each light beam passed through an interference filter tuned to one of three different wavelengths (538, 569 and 620 ± 10 nm; Asahi Spectra, Japan) and focused onto one of three video cameras by each projection lens. A combination of objective and projection lenses constituted the tandem-lens optics (Ratzlaff and Grinvald, 1991). Using different combinations of a projection lens (50 mm, f1.2; Nikon, Japan) and an objective lens (35 mm, f1.4 or 50 mm, f1.2; Nikon, Japan), imaging areas were 4.9 × 4.9 mm^2 or 7.0 × 7.0 mm^2 for the CID-2221D camera (256 × 256 pixels) and 8.8 × 6.6 mm^2 for the CS8310 camera (640 × 480 pixels). The imaging areas of the three cameras were adjusted to overlap in order to record signals from the same region of the cortical surface. Video signals from the three cameras were separately digitized with 10-bit video A/D converter boards (Pulsar, Matrox Graphics Inc., Canada) on three computers. These computers synchronously acquired 240 frames at a frame rate of 1/30 s for the CS8310 camera or 1/60 s for the CID-2221D camera. Fifteen consecutive frames for the CS8310 camera or 15 alternate frames for the CID-2221D camera were averaged on-line. Consequently, 16 images were acquired with a temporal resolution of 500 ms (i.e. 8 s). Acquired images were stored on hard disks without binning for the CID-2221D camera (256 × 256 pixels) and with binning (2 × 2 pixels were combined into a single pixel) for the CS8310 camera (i.e. 320 × 240 pixels).

Images of the cortical surface were taken using these cameras and the focal plane was changed from the cortical surface to 700–800 μm below. The maximum intensities of video signals from the three cameras were adjusted to near-saturation level by changing the intensity of incident light and camera gains. The black levels of each video signal (a video signal obtained under complete darkness, ~10% of saturation level) were then recorded for off-line data processing. In the experiment with anesthetized cats, data acquisition was started at a certain phase of respiration in synchrony with heartbeat. A visual stimulus appeared 1 s after the onset of image acquisition. To allow the relaxation of vascular responses to the previous stimulation, the interstimulus interval (ISI) was set at 30 s. Data of four trials using the same stimulus were averaged online and saved as one block. We recorded 20 blocks in one experiment; altogether, responses for 80 trials (20 blocks, 4 trials per block) were acquired for each stimulus.

In the recordings with awake cats, the body of the cat was placed into a loosely fitting pouch and the head was immobilized by the implanted head post. The cats quickly became accustomed to the restriction of movements and presented no signs of discomfort during the experiments. To minimize visual input from surroundings, the experiments were performed in a dark room and mechanical shutters were placed in front of the cat's eyes. The shutters were only opened during the stimulus presentation. Unlike the experiment under anesthesia, data acquisition was not synchronized with respiration and heartbeat. The total recording period was restricted to 1.5 h/day to maintain the cats' alertness level. Data from 40 trials were averaged (20 blocks, 2 trials per a block) for each stimulus in one day. The experiments were repeated for two successive days and the data from the two days were finally averaged. The temporal and spatial patterns of intrinsic signals on the first day were almost identical to those on the second day (data not shown). The data from the same cat under anesthesia were also collected. To ensure that recordings were taken from the same region, we did not change the camera position relative to the head post until a series of experiments for the cat had been completed. We did not observe a misalignment of cortical vascular patterns in the series of experiments.

Imaging of Changes in Blood Volume with Intravascular Absorption Dye

For the measurement of changes in blood volume, we injected a light-absorbing dye (Nigrosin, water-soluble Acid Black 2; Sigma) through the cat's cephalic vein and recorded the stimulus-evoked absorption changes at 620 nm. We chose absorption dye instead of fluorescent dyes, which have previously been used for the measurement of blood volume (Frostig *et al.*, 1990; Narayan *et al.*, 1995; Cannestra *et al.*, 1998), because (i) fluorescent dye signals are in general too weak to resolve small changes such as stimulus-specific components, (ii) there is minimal effect of dye bleaching, and (iii) the same optics can be employed to assess the dye-specific responses immediately after the intrinsic signal imaging. The dye was dissolved in saline, filtered using a Millipore filter (0.22 μm pore size, Millipore Co. Bedford, MA), and injected prior to recording (final dosage, 20–34 mg/kg nigrosin for five cats). The physiological conditions (e.g. heart rate) of the cats did not change following the injection of the dye. Since the dye absorbed the incident light, the reflected light intensity from the cortical surface decreased after the dye injection. The intensity of the reflected light was readjusted to the saturation level of video signals prior to recording by increasing the incident light intensity. Data from 20–80 trials were averaged (5 to 20 blocks, 4 trials per block) for each stimulus.

Data Analysis

We analyzed all images pixel by pixel using IDL 5.4 (Research Systems, Inc.). The statistical significance of the data was evaluated by *t*-test (two-tailed, paired). The first step in the data analysis was to extract reflected light intensity from video signals by subtracting the image obtained in complete darkness (the black level) from the 16 consecutive images (8 s at 0.5 s/image). A change in reflected light intensity (intrinsic signals) was then expressed as the change in the optical density (ΔOD) as follows:

$$\Delta OD(t)_\lambda = \ln\{I_\lambda^{pre}/I_\lambda(t)\} \quad (1)$$

where I_λ^{pre} is the average of reflected light intensity before stimulus onset (1 s) at a wavelength λ, and $I_\lambda(t)$ is the reflected light intensity at t s from the stimulus onset. We calculated ΔODs for the individual stimuli and for the control (blank screen), and then subtracted ΔOD for the control from ΔOD for the grating stimuli to remove artifacts due to the respiratory cycle.

To demonstrate the spatial patterns of iso-orientation domains, differential images were generated by subtracting responses to one orientation from those to the orthogonal orientation. The differential images were then temporally averaged from 1 to 7 s after stimulus onset and processed using a Gaussian spatial filter (cutoff frequencies, σ = 10/mm for a high cutoff frequency and 1/mm for a low cutoff frequency for images obtained by the CS8310 camera, and σ = 5/mm for high cut-off and 1/mm for low cutoff for images obtained by the CID-2221D camera). The similarity between two differential images obtained at different wavelengths was quantified by calculating a correlation coefficient on pixel-by-pixel basis. In particular, when two pairs of orthogonal stimuli (the combination of 0° and 90° or that of 45° and 135°) were used at these wavelengths, a correlation coefficient of differential images was calculated for each pair separately, and then an average of the correlation coefficients was used to evaluate the similarity of differential images obtained at these wavelengths.

To quantitatively examine the intensities of intrinsic signals we averaged pixels in the region of interest (ROI). Pixels covering surface vessels thicker than 50 μm and those located outside of the cortex were excluded from the ROI. We divided ROI into active and less-active domains and averaged pixels of the active domains separately from pixels of the less-active domains. The active and less-active domains were determined on the basis of a differential image at 620 nm processed with the spatial filter. Pixels having positive values in the

differential image were assigned to the active domains and the remaining pixels were assigned to the less-active domains. The difference in the signal intensity between two domains was calculated by subtracting the average pixel value for the less-active domains from that for the active domains.

To quantify the spatial resolution of intrinsic signals, we measured the distance between neighboring iso-orientation domains in differential images. The distance between neighboring iso-orientation domains in the differential image was evaluated using an auto-correlation map of the differential image using NIH Image software (Scion Corporation) since the pattern of iso-orientation domains seems to have a periodic structure. The differential image used for this analysis was not processed by any spatial filter. The autocorrelation map was calculated for an ROI of 128 × 128 pixels (2.5 × 2.5 mm^2 for the CID-2221D camera with a 35 mm objective lens and 3.5 × 3.5 mm^2 for the CID-2221D and CS8310 cameras with a 50 mm objective lens) in the differential images. We then extracted the profile of the autocorrelation map along the central and secondary largest peaks. We assigned the distance between these two peaks as the distance between neighboring iso-orientation domains assuming that the periodic structure of the iso-orientation domains is the most dominant one in the map. The size of iso-orientation domains was estimated by measuring full width at half-maximum (FWHM) of the center peak of the profile.

Results

Definition of Stimulus-specific and Stimulus-nonspecific Components of Intrinsic Signals

Figure 2*A,B* shows the spatiotemporal patterns of the intrinsic signal at 620 nm in cat visual cortex induced by full-field grating stimuli. The grating stimuli evoked initial increases in light absorption (darkening of the cortex), which were followed by absorption decreases across the baseline (lightening of the cortex). These absorption changes were not spatially confined to domains specific for particular stimulus orientations. As reported previously (Grinvald *et al.*, 1986), two orthogonal orientations elicited a common absorption increase over the entire range (stimulus-nonspecific component), which was locally modulated in a stimulus-specific manner (stimulus-specific component) (Fig. 2*D*). Since this stimulus-specific modulation is complementary in two orthogonal orientations (Fig. 2*D*, red and blue lines), the region showing this stimulus specificity was extracted by subtracting the response for one orientation from that for the orthogonal orientation (Fig. 2*C*, and Fig. 2*D*, green line). We define regions where a stimulus elicited a larger absorption than the orthogonal stimulus, such as the shaded regions shown in Figure 2*D*, as 'active domains' for the stimulus. On the other hand, we define regions where the stimulus elicited smaller increases in absorption than the orthogonal stimulus as 'less-active domains' for the stimulus. For the analysis of the stimulus-nonspecific component, we averaged the intrinsic signals regardless of whether the domain was active or less active. For the analysis of the stimulus-specific component, we subtracted the intrinsic signal for the less-active domains from the signal for the active domains (see also Materials and Methods).

Time Courses of Stimulus-nonspecific and Stimulus-specific Components of Intrinsic Signals

As an approximation, we assume that Hbr and HbO_2 concentration changes are the major sources of intrinsic signals at visible wavelengths. Intrinsic signals at 620 and 569 nm then correspond approximately to changes in Hbr concentration and that of total hemoglobin (Hbt) concentration (the sum of Hbr and HbO_2 concentrations), respectively. This is because at 620 nm, the absorption coefficient of Hbr is about 10 times larger than that of HbO_2 and 569 nm corresponds to the isosbestic point of Hbr and HbO_2 absorption (Fig. 1 inset). In addition, we recorded intrinsic signals at 538 nm, where HbO_2 has a higher absorption coefficient than Hbr. Figure 3*A* shows

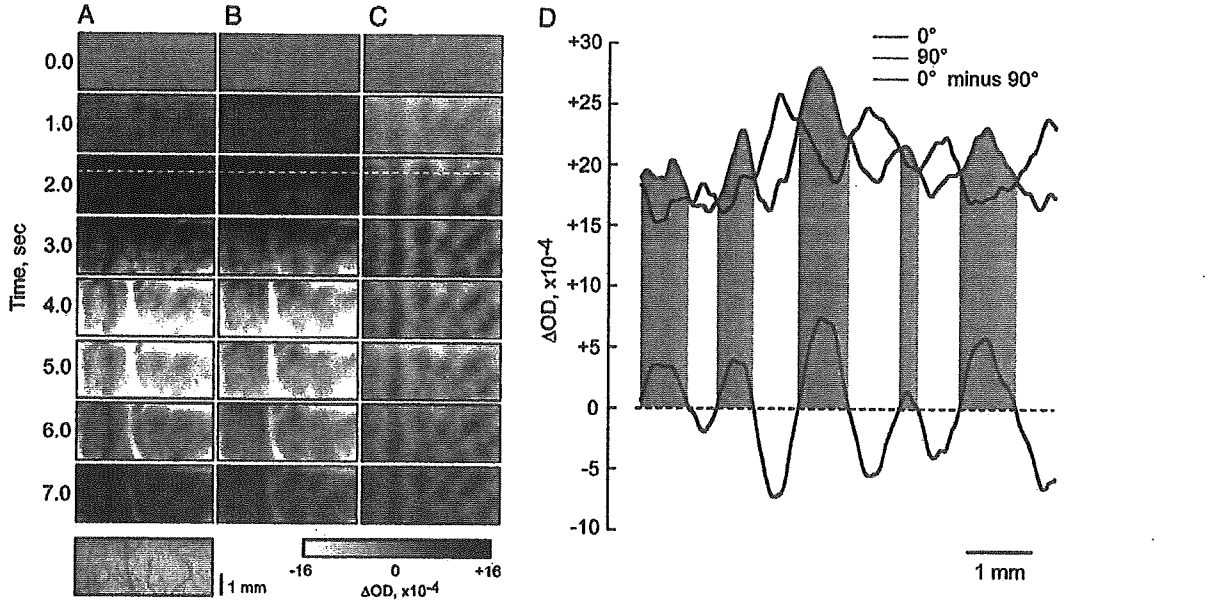

Figure 2. Stimulus-specific and stimulus-nonspecific components of intrinsic signals. (*A, B*) Images of intrinsic signal at 620 nm induced by gratings with 0° (*A*) and 90° (*B*) orientations along with the ROI at the bottom (cortical surface image taken at 538 nm). Grayscale range is shown at the bottom. The images are shown as a function of time from the stimulus onset. The stimulus duration was 2 s. (*C*) Differential images obtained by subtracting images in *B* from images in *A*. Black and white patches were specific to gratings of 0° and 90° orientations respectively. (*D*) Magnitudes of signal intensities along white broken lines on the images (*A–C*) at 2.0 s after stimulus onset. The horizontal broken line indicates the baseline corresponding to the absence of absorption change. Shaded regions indicate the portions showing larger responses to a grating at 0° orientation. The high-frequency noise of the lines was removed using the high-cut filter (cutoff frequency σ = 10/mm).

the time courses of stimulus-nonspecific components of the intrinsic signals obtained at these wavelengths. At 620 nm, we consistently observed biphasic time courses, in which the light absorption increased after stimulus onset, reached a maximum after 2 s and decreased, going below the baseline (time to reach the minimum, 5 s). On the other hand, the time courses of the signals at 538 and 569 nm were monophasic: the light absorption increased and returned to the baseline without crossing it (time to reach the maximum, 3.5 s). In accordance with the absorption coefficients of hemoglobin at 538 and 569 nm, light absorption changes at 538 nm were slightly larger than those at 569 nm. The biphasic time course of the signal at 620 nm suggests that Hbr concentration initially increased due to oxygen consumption of activated neurons, which was followed by a decrease in Hbr concentration below the baseline due to blood inflow outstripping oxygen consumption. On the other hand, the absorption increase at 569 nm can be explained by the increase in Hbt resulting from the increase in blood inflow.

Spatial Patterns of Stimulus-specific Component of Intrinsic Signals

Unlike the stimulus-nonspecific components of the intrinsic signals, the polarity of the stimulus-specific components did not change at these wavelengths (Fig. 3*B*). Thus, to visualize the spatial patterns of the stimulus-specific components, we first temporally averaged the intrinsic signals from 1 to 7 s after stimulus onset. Then, the differential images of the signals were calculated by subtracting the temporally averaged images for one orientation from those for the orthogonal orientation (Fig. 4*A*). Even if the physiological sources of the signals seem to be different among these wavelengths, the spatial patterns of the stimulus-specific components were almost identical. The correlation coefficients between the differential images obtained at 620 nm and those at other wavelengths calculated on a pixel-by-pixel basis were significantly high (0.86 and 0.90 for the images obtained at 538 and 569 nm respectively; $P < 0.01$). We obtained consistent results for the other 13 cats: the average correlation coefficients for the 14 cats were 0.78 ± 0.08 for the images at 538 nm and 0.71 ± 0.09 for the images at 569 nm. These values indicate that there is a statistically significant correlation between differential images obtained at 620 nm and those obtained at other wavelengths ($P < 0.01$). These results indicate that the intrinsic signals recorded at these three wavelengths have a sufficient spatial resolution to resolve orientation-specific columnar organizations.

To estimate their spatial resolution quantitatively, we calculated the distance between neighboring iso-orientation domains and the size of the domains from the autocorrelation maps of differential images (see Materials and Methods). Figure 4*B* shows an example of the autocorrelation map of a differential image at 569 nm and its spatial profiles along the broken line that connects the central and adjacent peaks. In this example, the distance between neighboring iso-orientation domains was estimated to be 1.38 mm from the profile, and the full width at half-maximum (FWHM) of the profile's central peak was 0.65 mm. The average spatial separation between iso-orientation domains for the 14 cats was 1.34 ± 0.29 mm, and the average FWHM was 0.58 ± 0.12 mm (mean ± SD). Accordingly,

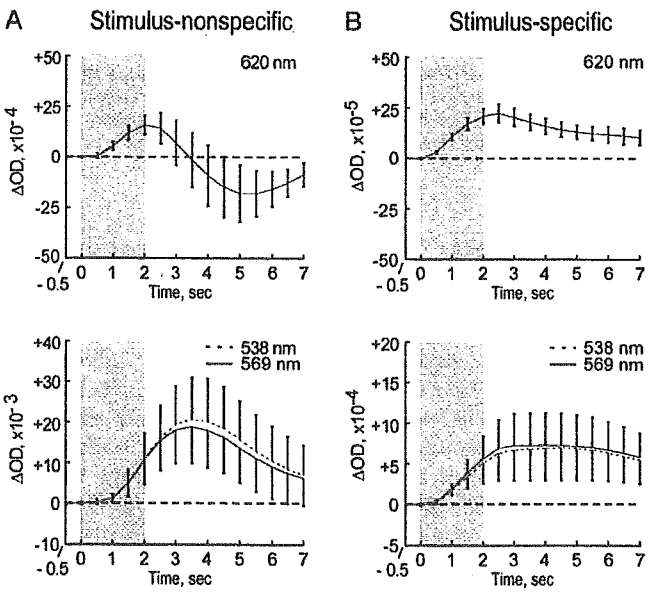

Figure 3. Time courses of stimulus-nonspecific and stimulus-specific components of intrinsic signals. (*A*) Time courses of intrinsic signals for stimulus-nonspecific components. Upper panel: 620 nm, Lower panel: 538 nm (dotted line) and 569 nm (solid line). (*B*) Time courses of intrinsic signals for stimulus-specific components. Upper panel: 620 nm, Lower panel: 538 nm (dotted line) and 569 nm (solid line). Error bars indicate one standard deviation (SD) of mean obtained from 14 cats. The shaded region indicates the duration of stimulus presentation. The horizontal broken line indicates the baseline corresponding to no absorption change.

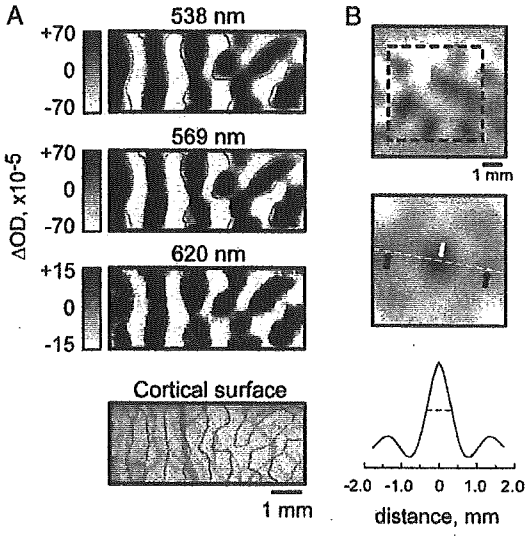

Figure 4. Spatial patterns of stimulus-specific components of intrinsic signals. (*A*) Differential images obtained from intrinsic signals at three wavelengths. The images were obtained by subtracting the responses to a grating at 90° orientation from those to a grating at 0° orientation. Black and white patches are specific to gratings at 0° and 90° orientations, respectively. Borders between active and less-active domains at 620 nm (red lines) are superimposed on each panel. This result and the result in Figure 2 were obtained from the same cortical ROI. (*B*) The analysis of spatial separations of neighboring iso-orientation domains and the domain sizes. Top panel: a differential image at 569 nm, where black and white patches are specific to gratings at 0° and 90° orientations, respectively. The grayscale range of ΔOD is $\pm 3.7 \times 10^{-4}$. The dotted rectangle (3.5×3.5 mm^2) in the differential image indicates the ROI for the analysis. Middle panel: the autocorrelation map of the ROI. White and black arrows indicate the largest peak (central peak) and secondary largest peaks on the map, respectively. Bottom panel: the spatial profile of the autocorrelation map along the broken line in the middle panel. The horizontal broken line in this profile indicates the FWHM of the central peak.

the spatial resolution of intrinsic signals at 569 nm was as high as 0.58 mm.

Measurement of Blood Volume Changes Based on Dye-specific Absorption Changes

Since intrinsic signals at 569 nm are considered to be proportional to Hbt concentration, the above analysis indicates that the blood volume component, as well as the Hbr component, has sufficient spatial precision to visualize individual iso-orientation domains in areas 17 and 18 of the cat visual cortex.

To further confirm our interpretation, we injected an absorption dye into the bloodstream and measured changes in blood volume on the basis of dye-specific absorption changes. Three observations provided evidence that the dye-specific absorption changes reflected changes in blood volume. First, the injections of the dye into the bloodstream caused a 17 ± 3% (mean ± SD, $n = 5$ cats) increase in light absorption. Second, the dye injections also increased the amplitude of the stimulus-nonspecific component of changes in absorption (Fig. 5*A*). The ratio of peak amplitudes before and after injections was 2.1 ± 1.1 (mean ± SD, $n = 5$). Thirdly, we found that the time courses of the stimulus-nonspecific component for the intrinsic signal at 569 nm were the same as those for the dye-specific absorption changes (Fig. 5*B*).

To examine whether stimulus-specific changes in blood volume are confined to iso-orientation domains, we compared differential images obtained before and after the dye injection (Fig. 6). If there were no stimulus-specific changes in blood volume, there would be no change in the differential image. However, the contrast of black and white patches in the differential image was in fact enhanced by the injection (Fig. 6*A*). For example, the magnitudes of stimulus-specific modulations became larger after the dye injection (Fig. 6*B*). We obtained similar results from all five cats. To quantify the results, we calculated the spatial and temporal averages (from 1 to 7 s after stimulus onset) of the stimulus-specific component of the intrinsic signals before and after the injections, and the magnitudes of the stimulus-specific components after the injections (vertical axis) were plotted against those before the injections (horizontal axis). As shown in Figure 6*C*, the magnitudes of the stimulus-specific components increased after dye injection in all five cats. These results support the proposal that there are stimulus-specific changes in blood volume.

Contribution of Changes in Blood Volume to the Intrinsic Signals in Awake Cats

To examine the blood volume component of intrinsic signals also in awake cats, we compared the intrinsic signals at 569 nm in anesthetized and awake states from the same cat. To avoid the effect of eye movements following the grating stimulus motion on the intrinsic signal in the awake state, we recorded the signal evoked by a flickering grating stimulus instead of a moving grating stimulus both in anesthetized and awake states in this experiment. We confirmed beforehand that these two stimuli elicited nearly the same responses in temporal patterns and identical response in the spatial patterns of iso-orientation domains in anesthetized cats (data not shown).

The time courses of intrinsic signals at 569 nm in the awake state were similar to those in the anesthetized state. The time to

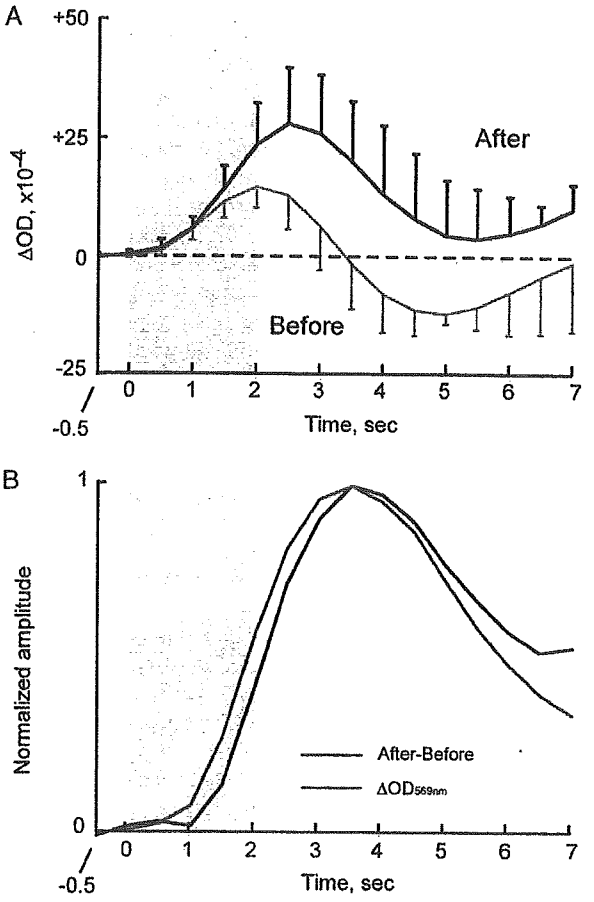

Figure 5. Contribution of blood volume changes to intrinsic signals. (*A*) Time courses of stimulus-nonspecific components of intrinsic signals at 620 nm before (orange line) and after (black line) dye injection. Error bars indicate one SD of mean obtained from five cats. (*B*) Comparison between the time course of intrinsic signals at 569 nm (green line) and that of dye-specific absorption changes (black line). Dye-specific absorption change was obtained by subtracting the absorption change at 620 nm before the injection (orange line in *A*) from that after the injection (black line in *A*). Each signal was normalized to their maximum values for comparison. The intrinsic signal at 569 nm shown here is the same data as in those shown in Figure 3*A*.

reach the peak (mean ± SD, $n = 5$ cats) of the intrinsic signal at 569 nm was 4.2 ± 0.6 s in the anesthetized state and 4.1 ± 0.46 s in the awake state. The spatial patterns of iso-orientation domains revealed by differential images at 569 nm in both states were almost identical (Fig. 7). Quantitatively, the correlation coefficient between the two images was 0.77 in this example. This value and the correlation coefficients obtained from the other four cats indicate that there is a statistically significant correlation between these images [average correlation coefficient: 0.74 ± 0.11 (mean ± SD); $P < 0.01$]. The average distance between neighboring iso-orientation domains and the average FWHM for the five awake cats was 1.26 ± 0.31 and 0.60 ± 0.10 mm respectively (mean ± SD). These values are similar to those obtained from the above-mentioned anesthetized cats. These results suggest that stimulus-specific changes in blood volume are not specific to the anesthetized state.

A difference in the intrinsic signal between the anesthetized and awake states was the magnitude of the stimulus-nonspecific and -specific components (Fig. 8). Figure 8*A* shows the average signal magnitude when the intrinsic signal at 569 nm reached its

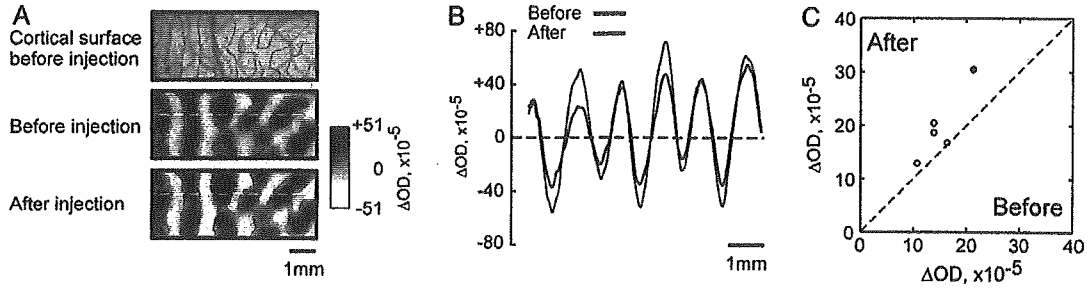

Figure 6. Stimulus-specific blood volume changes revealed by dye-specific absorption changes. (*A*) Spatial patterns of iso-orientation domains revealed by differential images before and after dye injection. The images were obtained by subtracting the responses to a grating at 90° orientation from those to a grating at 0° orientation and were temporally averaged from 1 to 7 s after stimulus onset. Borders between active and less-active domains before the injection (red lines) are superimposed on each panel. (*B*) Changes in signal intensities along the broken lines in the differential images of *A*. Black and red lines are the spatial profiles of stimulus-specific components before and after the dye injection, respectively. This result and the result shown in Figures 2 and 4*A* were obtained from the same cortical ROI. (*C*) The average magnitude of stimulus-specific components before (*x*-axis) and after (*y*-axis) the injection are plotted for five cats. Filled circle represents the result for the cat used in obtaining data shown in *A* and *B*.

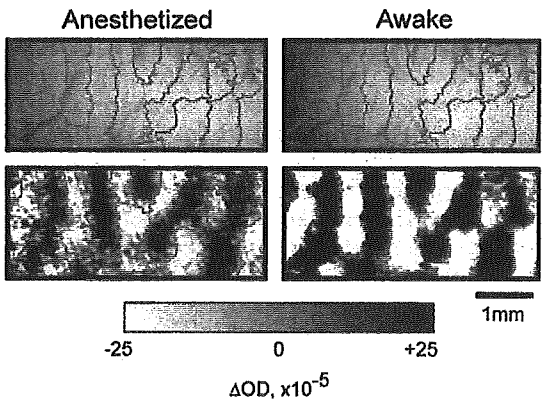

Figure 7. Maps of iso-orientation domains obtained from a cat in anesthetized and awake states. Upper panels: images of cortical surfaces taken at 538 nm from the same recording area in anesthetized and awake states. Lower panels: maps of iso-orientation domains revealed by differential images of intrinsic signals at 569 nm. The differential images were obtained by subtracting the responses evoked by an 8 Hz flickering grating at 90° orientation from the responses to a grating at 0° orientation and were temporally averaged from 1 to 7 s after stimulus onset. Borders between active and less-active domains at 569 nm in awake state (green lines) are superimposed on each panel. Recording from the anesthetized cat was conducted two days after that from the awake cats.

maximum (n = 5 cats). In the anesthetized state, neural activation induced increases in light absorption both in active and less-active domains corresponding to the stimulus-nonspecific component of the signals (Fig. 8*A*). The average magnitude of the stimulus-nonspecific component for the five cats was 15.7 × 10^{-3} in ΔOD. The increases in light absorption were always, though slightly, larger in the active domains of individual cats as shown by the difference in intrinsic signals between active and less-active domains (Fig. 8*B*). This difference corresponds to the stimulus-specific component of the intrinsic signal. The average magnitude of the stimulus-specific components for the five cats was 3.6 × 10^{-4} in ΔOD. Thus, the stimulus-specific component was only 2.3% of the stimulus-nonspecific component. The stimulus-nonspecific and stimulus-specific components of the intrinsic signal in the awake state were larger than those in the anesthetized state: the average magnitude of the stimulus-nonspecific components was 2.7 times larger and the average magnitude of stimulus-specific components was 3.6 times larger (Fig. 8*C*). The difference in magnitude ratio (2.7 versus 3.6) between stimulus-nonspecific and stimulus-specific components suggests that these two components have a different sensitivity to anesthesia.

Discussion

Spatial Localization of Changes in Blood Volume Elicited by Neural Activation

Several studies revealed the submillimeter-scale spatial localization of Hbr concentration changes in visual cortex (Malonek and Grinvald, 1996; Kim *et al.*, 2000; see also Thompson *et al.*, 2003). In this study, we examined the spatial precision of changes in blood volume using two different methods of analyzing reflection changes elicited by neural activation: (i) intrinsic signal imaging at the wavelength of the isosbestic point of hemoglobin, and (ii) analysis of stimulus-induced absorption changes of an intravenously infused dye. These analyses provide concrete evidence supporting a previous proposal that changes in blood volume are spatially localized (Frostig *et al.*, 1990). We showed that blood volume, as well as Hbr concentration, is precisely controlled at a submillimeter-scale resolution in areas 17 and 18 of the cat visual cortex in anesthetized and awake states.

It should be pointed out that a blood volume increase includes an intravascular space increase accompanied by the dilation of vessels (increase in plasma volume) and an increase in the number of red blood cells. The measurement of the intrinsic signal at 569 nm is sensitive to the increase in the number of red blood cells. On the other hand, it is considered that the increase in dye-specific absorption change reflects the increase in plasma volume. However, we cannot exclude the possibility that the dye-specific responses also reflect the increased number of red blood cells, since we did not quantitatively examine the possibility that the dye molecules were accumulated in or bound to red blood cells. Taking into account a previous *in vivo* microscopy study (Villringer *et al.*, 1994) demonstrating that increase of red blood cells in a capillary is associated with capillary dilation (i.e. increase of plasma volume) during hypercapnia, it is more plausible that these two effects — the increase in intravascular space and the increase in the number of red blood cells — are coupled and show similar behavior even when these changes are elicited by neural activation.

From the measurement of spatial separation and the size of the iso-orientation domains, we estimated the spatial resolution of blood volume changes to be as high as 0.6 mm. Recently,